Tomographic Imaging for Orbital Radar Sounding of Earth's Ice Sheets

Min Liu , Peng Xiao , *Member, IEEE*, Lu Liu , Xiaohong Sui , and Chunzhu Yuan

Abstract—BingSat-Tomographic Observation of Polar Ice Sheets (BingSat-TOPIS) is a spaceborne multistatic radar sounding system that can achieve high resolution and stereoscopic observation. It is designed to penetrate ice sheets and acquire tomographic image. The satellite group fly over the Polar Regions, which can form about 6.56-km cross-track baseline. This cross-track baseline is formed by one master satellite and 40 slave CubeSats. In this article, we propose a tomographic imaging algorithm for orbital radar sounding of the Earth's ice sheets. First, we give the method to calculate the two-way slant range in air and ice. The phase errors of the method are smaller than $\pi/4$ rad. Second, we express the radar data cube for a point target in ice sheets. The radar data cube is made of 40 bistatic synthetic aperture radar echo signals. At last, the echoes are simulated for the TOPIS system, and a matched filter is used for pulse compression in range. Then, the back projection algorithm is used in track and cross-track imaging. The experimental results demonstrate that our tomographic imaging algorithm is effective and reliable.

Index Terms—Back projection (BP), orbital radar sounding, polar ice sheets, tomographic imaging.

I. INTRODUCTION

ONE of the major purposes of the polar observation is to gather the information of ice mass in Polar Regions, which has an important influence on global climate change and sea level rise [1], [2], [3]. There are many kinds of radar sounding systems to monitor the losing mass of polar ice sheets [4], [5], [6], [7], [8]. Currently, vehicle-borne and airborne systems are the most commonly used platforms. They cost a lot of manpower and material resources. Besides, the update rate in time is still not enough. In the northern part of Greenland, it is reported that the sum of attenuation is more than 60 dB for 3-km thick interior ice [9]. Therefore, the radar sounding system called BingSat-Tomographic Observation of Polar Ice Sheets (BingSat-TOPISs) is proposed to achieve high resolution and stereoscopic observation [10]. It can get fine resolution in cross-track, along-track (track or azimuth), and vertical (range).

Min Liu, Peng Xiao, Lu Liu, and Xiaohong Sui are with the Qian Xuesen Laboratory of Space Technology, Beijing 100094, China (e-mail: ruiminlau@163.com; xiaopeng_email1984@163.com; lluiulluiu@126.com; suixiaohong@qxslab.cn).

Chunzhu Yuan is with the DFH Satellite Co., Ltd., China Academy of Space Technology, Beijing 100094, China (e-mail: yuanchunzhu123456@163.com).

For BingSat-TOPIS, it faces a lot of challenges [11]. This article is mainly focused on the tomographic imaging algorithm [12] for the internal layer in ice sheets, which is not just simple combination of 2-D (track × vertical) images dataset. BingSat-TOPIS has the following characteristics.

1) The transmit and receive antennas are separated (40 bistatic SARs).
2) The received signals travel through two media (air and ice).

In this article, we mainly propose a tomographic imaging algorithm for orbital radar sounding of Earth's ice sheets. In Section II, system formation of BingSat-TOPIS and some key parameters are described. Based on Earth observation geometry, the slant range and the signal model for BingSat-TOPIS are built in Section III. In this part, we give the equivalent slant range of a new model to improve computational efficiency, which only needs to calculate the quintic equation twice for a two-way slant range. The new model is used to reduce the computation time. The detailed description of simulation processing and tomographic imaging results is presented in Section IV. Finally, Section V concludes this article.

II. BRIEF INTRODUCTION FOR THE BINGSAT-TOPIS SYSTEM

BingSat-TOPIS is designed to realize a 100 m × 20 m × 5 m resolution (cross-track × track × vertical), which can compensate 65-dB ice attenuation and realize –3.5-dB system sensitivity [10]. It has sounded the ice depth about 4000 m. The system can realize the high-resolution tomographic imaging of polar ice sheets by combining various advanced technologies.

The vertical resolution ρ_v for the nadir-looking radar sounding system is given by

$$\rho_v \approx c_{\text{ice}}/(2B_r) = (c/\sqrt{\varepsilon_r})/(2B_r) \tag{1}$$

where c_{ice} is the speed of the electromagnetic wave in ice, c is the speed of light in vacuum, and B_r is the bandwidth of the transmitting signal.

The ice surface resolution ρ_a is defined as

$$\rho_a \approx D_a/2 \tag{2}$$

where D_a is the length of the azimuth antenna. The length of a 40-m diameter parabolic transmitting antenna is 40 m.

In the wavenumber domain, the cross-track spatial resolution ρ_c can be expressed as

$$\rho_c \approx \lambda/(\phi_i + \phi_e) \tag{3}$$

TABLE I
SYSTEM PARAMETERS OF BINGSAT-TOPIS

Parameter	Symbol	Value
Orbit altitude over polar	R_H	449 km (radius 6806.137 km)
Orbital inclination		90°±0.028° ($B_\perp$ > 6.56 km)
Wavelength	λ	1 m (300 MHz)
Cross-track resolution	ρ_c	100 m
Along-track resolution	ρ_a	20 m
Vertical resolution	ρ_v	5 m (in ice)
Bandwidth	B_r	17.5 MHz
Master antenna area	A_t	10^3 m^2 (diameter 40 m)
Slave antenna gain	G_r	9 dB (4 half-wavelength Dipoles)
Num. of slave satellites	N	40
Interval of slave satellites	$b_\perp$	164 m±50 m (1σ)
Average transmit power	P_{ave}	2200 W
Noise figure and losses	FL_{free}	5 dB
Detectability	σ_0/L_{ice}	-68.5 dB
Detectable SNR	SNR	5 dB

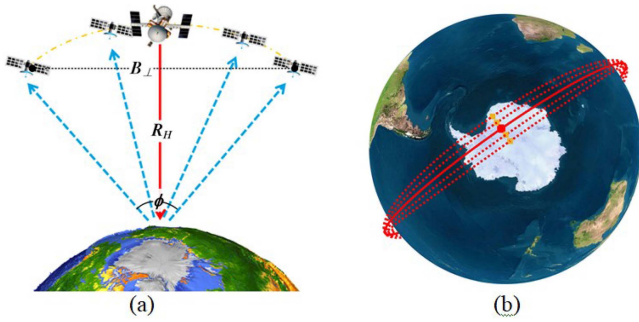Fig. 1. System formation of TOPIS [10]. (a) Long baseline realized by cross-track multistatic radar. (b) Orbits of the satellites.

III. SIGNAL MODEL FOR TOPISs

A. Slant Range Between Air and Ice

BingSat-TOPIS is different with the ground penetrating radar (GPR) system and airborne radar sounding system. For the satellite case, the rectilinear geometry is replaced by the curved Earth geometry. The orbits of the master and the slave satellites
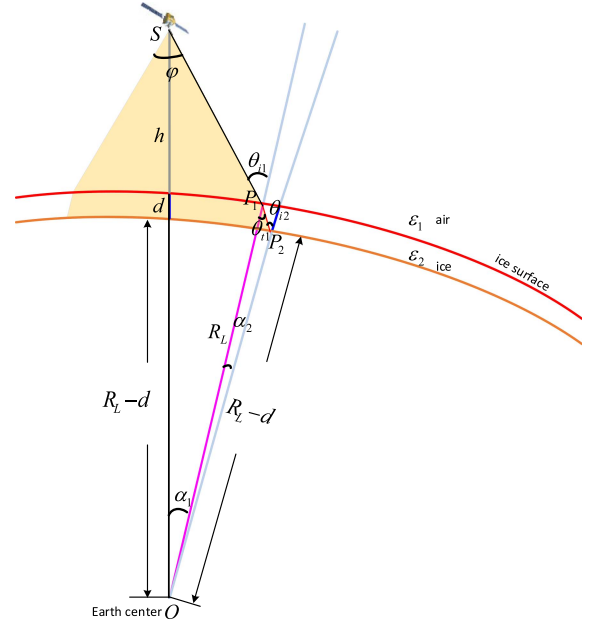

Fig. 2. One-way slant range geometry from satellite to a point target in ice.

are curved. The ice sheets on Earth are also curved. Besides, the Earth is rotating independently of the satellite orbit.

For BingSat-TOPIS, the master satellite in the middle is surrounded by 40 slave satellites. It carries a high transmitting power antenna, which is vertical observation. The slave satellites each carries a dipole receiving antenna and receives the radar echo from Earth. In this article, unless otherwise stated, all parameters are expressed in Earth centered rotating (ECR) coordinates.

BingSat-TOPIS is composed of 40 bistatic SAR configurations. A bistatic SAR configuration is chosen and analyzed. First, an accurate equation of slant range is deduced. Based on the accurate equation, a quintic equation for one-way slant range is presented with shorter computation time than the accurate equation.

Geometry of slant range (one-way) between antenna and a point target in ice sheets is illustrated in Fig. 2. As shown in Fig. 2, S represents the position of the satellite, φ is the cross-track beamwidth, h is the height of the satellite, O is set as the Earth's center, and R_L is the local radius of the Earth. There is a target P_2, whose ice depth is d. P_1 is the incident point at air–ice interface between the satellite S and the target P_2. θ_{i1} and θ_{t1} are the angle of incidence and the angle of refraction at P_1, respectively. θ_{i2} is the angle of incidence at P_2. α_1 and α_2 are the angles for $\angle SOP_1$ and $\angle P_1OP_2$, respectively. ε_1 and ε_2 are the dielectric constant of air and the dielectric constant of ice, respectively.

Assuming t_i is the azimuth time, $\boldsymbol{R}_s(t_i) = [R_{sxi}, R_{syi}, R_{szi}]$ and $\boldsymbol{P}_2 = [P_{2x}, P_{2y}, P_{2z}]$ are the position vectors for S and P_2, respectively. The local radius R_L is given by [13]

$$R_L = \frac{R_e R_p}{\sqrt{R_p^2 \cos^2 \Phi_s + R_e^2 \sin^2 \Phi_s}} \qquad (5)$$

where ϕ_i is the range of the incident angle, and ϕ_e is the range of the emergence angle. In the single-input and multiple-output (SIMO) formation, the range of the incident angle ϕ_i is zero, and the range of the emergence angle ϕ_e depends on the maximum cross-track baseline $B_\perp$. Therefore, ρ_c becomes

$$\rho_c \approx \lambda \left(R_H + d/\sqrt{\varepsilon_r} \right)/B_\perp. \qquad (4)$$

Table I gives the system parameters of BingSat-TOPIS [10].

As shown in Fig. 1(a), the master satellite in the center of the formation carries a large transmitting antenna, and the 40 slave satellites receive the echoes together and retransmit them to the master satellite for sampling and recording. In Fig. 1(b), in order to reach the Polar Regions simultaneously and keep a stable baseline, all satellites must fly in nearly circular with only small differences in eccentricity.

where R_e and R_p are the semimajor axis and the semiminor axis of the Earth, respectively. The geocentric latitude Φ_s is given by

$$\Phi_s = \arctan\left(\frac{R_{szi}}{\sqrt{R_{sxi}^2 + R_{syi}^2}}\right). \qquad (6)$$

The distance between the satellite S and the Earth's center O is given by

$$R_{sg} = \sqrt{R_{sxi}^2 + R_{syi}^2 + R_{szi}^2}. \qquad (7)$$

The distance between the target P_2 and the Earth's center O is given by

$$R_{tg} = \sqrt{P_{2x}^2 + P_{2y}^2 + P_{2z}^2}. \qquad (8)$$

Considering microwave propagates in air, the slant range between the satellite S and the target P_2 is given by

$$R_{st} = \sqrt{(R_{sxi} - P_{2x})^2 + (R_{syi} - P_{2y})^2 + (R_{szi} - P_{2z})^2}. \qquad (9)$$

α is the angle for $\angle SOP_2$. According to the cosine law, α is given by

$$\alpha = \text{acos}\left(\frac{R_{sg}^2 + R_{tg}^2 - R_{st}^2}{2R_{sg}R_{tg}}\right). \qquad (10)$$

Considering microwave propagates between air and ice, the slant range is divided into slant range of air and slant range of ice. As shown in Fig. 2, the angle of incidence θ_{i1} is expressed as

$$\sin\theta_{i1} = \frac{R_{sg} \cdot \sin\alpha_1}{\sqrt{R_{sg}^2 + R_L^2 - 2R_{sg}R_L\cos\alpha_1}} \qquad (11)$$

where the denominator is the distance between S and P_1.

Similarly, the angle of incidence θ_{i2} can be expressed as

$$\sin\theta_{i2} = \frac{R_L \cdot \sin\alpha_2}{\sqrt{R_L^2 + R_{tg}^2 - 2R_L R_{tg}\cos\alpha_2}} \qquad (12)$$

where the denominator is the distance between P_1 and P_2. The relationship between the angle of incidence θ_{i2} and the angle of refraction θ_{t1} is given by

$$\theta_{t1} = \theta_{i2} - \alpha_2. \qquad (13)$$

Substituting (12) into (13), $\sin\theta_{t1}$ is written as

$$\begin{aligned}\sin\theta_{t1} &= \sin\left(\theta_{i2} - \alpha_2\right) \\ &= \sin\left(\arcsin\left(\frac{R_L \cdot \sin\alpha_2}{\sqrt{R_L^2 + R_{tg}^2 - 2R_L R_{tg}\cos\alpha_2}}\right) - \alpha_2\right).\end{aligned} \qquad (14)$$

According to Snell's law, the refractive index of the ice layer can be written as

$$\begin{aligned}n_{\text{ice}} &= \frac{\sin\theta_{i1}}{\sin\theta_{t1}} \\ &= \frac{\frac{R_{sg}\cdot\sin(\alpha - \alpha_2)}{\sqrt{R_{sg}^2 + R_L^2 - 2R_{sg}R_L\cos(\alpha - \alpha_2)}}}{\sin\left(\text{a}\sin\left(\frac{R_L\cdot\sin\alpha_2}{\sqrt{R_L^2 + R_{tg}^2 - 2R_L R_{tg}\cos\alpha_2}}\right) - \alpha_2\right)}.\end{aligned} \qquad (15)$$

Here, the aforementioned equation (15) is an accurate equation of slant range between air and ice.

α_2 is much smaller than α_1. If α_2 is ignored, (15) can be rewritten as

$$\begin{aligned}n_{ice} &= \frac{\sin\theta_{i1}}{\sin\theta_{t1}} \approx \frac{\sin\theta_{i1}}{\sin\theta_{i2}} \\ &= \frac{\frac{R_{sg}\cdot\sin(\alpha - \alpha_2)}{\sqrt{R_{sg}^2 + R_L^2 - 2R_{sg}R_L\cos(\alpha - \alpha_2)}}}{\frac{R_L\cdot\sin\alpha_2}{\sqrt{R_L^2 + R_{tg}^2 - 2R_L R_{tg}\cos\alpha_2}}}\end{aligned} \qquad (16)$$

where $\theta_{t1} = \theta_{i2} - \alpha_2 \approx \theta_{i2}$. Squaring both sides of (16), we obtain

$$\begin{aligned}&\frac{R_{sg}^2\sin^2(\alpha - \alpha_2)}{R_{sg}^2 + R_L^2 - 2R_{sg}R_L\cos(\alpha - \alpha_2)} \\ &= \frac{n_{ice}^2 R_L^2 x^2}{R_L^2 + R_{tg}^2 - 2R_L R_{tg}\sqrt{1 - x^2}}\end{aligned} \qquad (17)$$

letting $\sin\alpha_2 = x$ and $\sqrt{1 - x^2} \approx 1 - \frac{x^2}{2}$. If the ice depth $d \neq 0$, a quintic equation is expressed as where the solution x can be obtained by solving the quintic equation. Thus, α_2 is easily obtained through x.

For BingSat-TOPIS, it involves only a very small error between the quintic (18) shown at the bottom of this page and the accurate (15). However, the computation time using (18) is much faster than using (15).

However, the quintic (18) and the accurate (15) are both very time consuming. We need to find a way to solve this problem.

The slant range errors for a bistatic SAR in BingSat-TOPIS are shown in Fig. 3. The receiving satellite of the bistatic SAR has the farthest distance to the master satellite. As shown in Fig. 3, the maximum slant range error of the bistatic SAR in BingSat-TOPIS is no more than 0.001 m.

B. Equivalent Slant Range by Rectilinear Geometry

As shown in Fig. 4, the blue dots S and S_c represent the position of the satellite at the azimuth time t_i and $t_c = 0$, respectively. The red dot P represents the position of the point target. S_c, S_{surf}, S_d, S_v, P_c, P_{surf}, P, and P_v are on the zero Doppler plane. The lines of $\overline{P_c S_c}$, $\overline{P_{\text{surf}} S_{\text{surf}}}$, $\overline{PS_d}$, and $\overline{P_v S_v}$ are perpendicular to the line of $\overline{S_c S_v}$, and their perpendicular

$$\begin{aligned}&R_{sg}^2\sin\alpha\cdot\cos\alpha R_L R_{tg}\cdot x^5 + \left(R_{sg}^2\cos2\alpha R_L R_{tg} - n_{ice}^2 R_L^3 R_{sg}\cos\alpha\right)\cdot x^4 \\ &+ \left(R_{sg}^2\sin\alpha\cdot\cos\alpha\cdot d^2 - 2R_{sg}^2\sin\alpha\cdot\cos\alpha\cdot R_L R_{tg} + 2n_{ice}^2 R_{sg}\cdot R_L^3\sin\alpha\right)x^3 \\ &+ \left[R_{sg}^2\left(\sin^2\alpha\cdot R_L R_{tg} + \cos2\alpha\cdot d^2\right) - n_{ice}^2 R_L^2\left(R_{sg}^2 + R_L^2 - 2R_{sg}R_L\cos\alpha\right)\right]x^2 \\ &- 2R_{sg}^2\sin\alpha\cdot\cos\alpha\cdot d^2\cdot x + R_{sg}^2\sin^2\alpha\cdot d^2 = 0\end{aligned} \qquad (18)$$
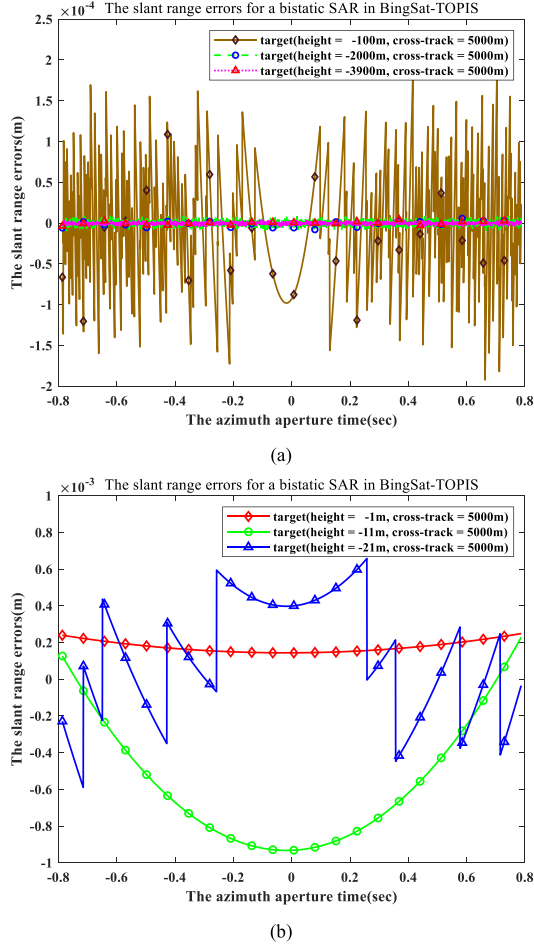
Fig. 3. Slant range errors for a bistatic SAR in BingSat-TOPIS.

Fig. 4. Rectilinear geometry of slant range between a satellite and a point target in ice.

distances are the same. h is the height of satellite, d is the ice depth, d_{eq} is the equivalent virtual depth, and v is called effective radar velocity. $t_c = 0$ is the time of closest approach. t_i is the azimuth time referenced to the time of closest approach. At the azimuth time $t_c = 0$, the equivalent slant range is the sum of slant range in air $R_{air}(0,d)$ and slant range in ice $R_{ice}(0,d)$. At the azimuth time $t_c = 0$, l_c is distance between the point of incidence and the point of refraction on the ice surface, and z_c is distance between the point of incidence and the nadir of the satellite on the ice surface. Similarly, we define t_i, $R_{air}(t_i,d)$, $R_{ice}(t_i,d)$, l, and z. At the azimuth time t_i, θ_i is the angle of incidence, and θ_t is the angle of refraction.

At the azimuth time $t_c = 0$, $Z_c = l_c + z_c$.

At the azimuth time t_i, the slant range between a satellite and a point target in ice is given by

$$R(t_i, d) = R_{air}(t_i, d) + n_{ice} \cdot R_{ice}(t_i, d). \tag{19}$$

As shown in Fig. 4, $R_{air}(t_i,d)$ and $R_{ice}(t_i,d)$ are given by

$$R_{air}(t_i, d) = \sqrt{h^2 + \left(\sqrt{(x + Z_c)^2} - l\right)^2} \tag{20}$$
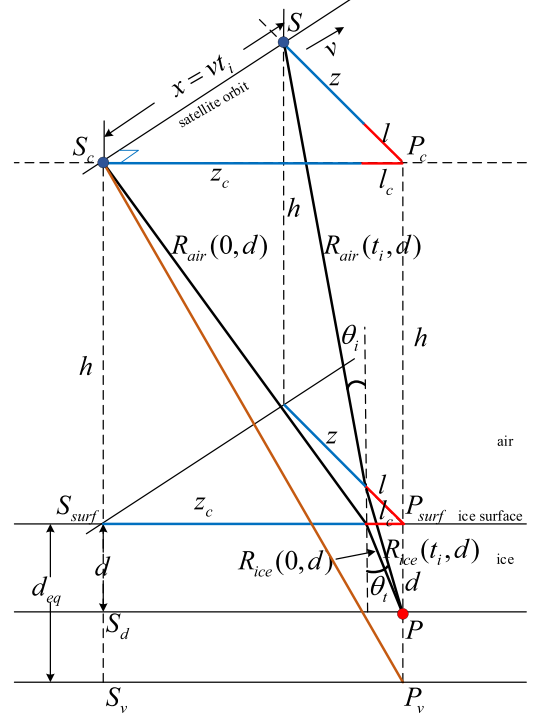
$$R_{ice}(t_i, d) = \sqrt{d^2 + l^2} \tag{21}$$

where x and l vary with the azimuth time t_i.

The first derivative of the slant range is given by

$$\frac{dR(t_i, d)}{dt_i} = \frac{dR_{air}(t_i, d)}{dt_i} + \frac{n_{ice} \cdot dR_{ice}(t_i, d)}{dt_i}. \tag{22}$$

If $Z_c = 0$, we obtain [14]

$$\left.\frac{dR(t_i, d)}{dt_i}\right|_{Z_c=0, t_i=0} = v \cdot \sin\theta_i = v \cdot \frac{x - l}{\sqrt{h^2 + (x - l)^2}} = 0. \tag{23}$$

The second derivative of the slant range is written as

$$\left.\frac{d^2 R(t_i, d)}{dt_i^2}\right|_{Z_c=0, t_i=0} = \frac{d\left[v \cdot \frac{x-l}{\sqrt{h^2+(x-l)^2}}\right]}{dt_i} = \frac{v^2}{R_{air}(0, d)}. \tag{24}$$

If $Z_c \neq 0$, using $\sin\theta_i = n_{ice} \cdot \sin\theta_t$, (20) becomes

$$\left.\frac{dR(t_i, d)}{dt_i}\right|_{Z_c\neq0, t_i=0} = \frac{v^2 t_i - \frac{v^2 t_i \cdot l}{\sqrt{v^2 t_i^2 + Z_c^2}}}{R_{air}(t_i, d)} = 0. \tag{25}$$

The second derivative of the slant range is written as

$$\left.\frac{d^2 R(t_i, d)}{dt_i^2}\right|_{Z_c\neq0, t_i=0} = \frac{d\left[\frac{v^2 t_i - \frac{v^2 t_i \cdot l}{\sqrt{v^2 t_i^2 + Z_c^2}}}{R_{air}(t_i, d)}\right]}{dt_i}$$

$$= \frac{v^2 \cdot (Z_c - l_c)}{R_{air}(0, d) \cdot Z_c}. \tag{26}$$

For the rectilinear geometry, the height of satellite h and the ice depth d are both constants. The beam footprint on Earth's surface for the master satellite can be written as

$$W = \beta \cdot h = 0.886 \frac{\lambda}{L} \cdot h. \tag{27}$$

Substituting $\lambda = 1\text{m}$, $h = 449\text{km}$, and $L = 40\text{m}$ into (27), we obtain

$$Z_{c,\max} = \frac{W}{2} = 0.886 \frac{\lambda h}{2L} \tag{28}$$

where $Z_{c,\max}$ is about 5 km for the master satellite.

The master satellite is vertical observation (449 km), the ice depth is 4 km, and the maximum cross-track $Z_{c,\max}$ is about 5 km. There are two ways to calculate the equivalent slant range by using the rectilinear geometry of Fig. 4.

1) The equivalent slant range between a satellite and a virtual point P_v in air

$$R(t_i) = \sqrt{\left[(h+d_{\text{eq}})^2 + Z_c^2\right] + (vt_i)^2} = \sqrt{R_c^2 + (vt_i)^2} \tag{29}$$

where $R_c = \sqrt{(h+d_{\text{eq}})^2 + Z_c^2} = R_{\text{air}}(0,d) + n_{\text{ice}} \cdot R_{\text{ice}}(0,d)$ is the closest approach. The second derivative of the equivalent slant range is written as

$$\frac{d^2 R(t_i)}{dt_i^2} = \frac{v^2}{R_c}. \tag{30}$$

Comparing (26) and (30), their second derivatives have a little difference.

2) The equivalent slant range of a new model

For the satellites of BingSat-TOPIS, $R_{\text{air}}(0,d) \gg v_{\text{eq}}t_i \gg l_{\text{eq}}$, and l_{eq} is varies with $v_{\text{eq}}t_i$. The equivalent slant range in air is written as

$$R_{\text{air\_eq}}(t_i, d)$$
$$= \sqrt{R_{\text{air}}(0,d)^2 + (v_{\text{eq}}t_i - l_{\text{eq}})^2 + 2R_{\text{air}}(0,d)(v_{\text{eq}}t_i - l_{\text{eq}})\sin\phi_{\text{squ}}} \tag{31}$$

where v_{eq}, l_{eq}, and ϕ_{squ} are the equivalent velocity, equivalent length, and equivalent squint angle, respectively.

The equivalent slant range in ice is written as

$$R_{\text{ice\_eq}}(t_i, d) = \sqrt{R_{\text{ice}}(0,d)^2 + l_{\text{eq}}^2}. \tag{32}$$

According to (9), v_{eq} is given by

$$v_{\text{eq}} = \frac{1}{2}\left[\frac{\sqrt{R_{st}^2(t_{i\_\text{start}}, d) - R_{st}^2(0,d)}}{|t_{i\_\text{start}} - 0|}\right. \\ \left. + \frac{\sqrt{R_{st}^2(t_{i\_\text{stop}}, d) - R_{st}^2(0,d)}}{|t_{i\_\text{stop}} - 0|}\right] \tag{33}$$

where t_{i_start} and t_{i_stop} are the start and stop time of azimuth.

The equivalent length l_{eq} is given by

$$l_{\text{eq}} = \varepsilon \cdot v_{\text{eq}}t_i = \frac{R_{\text{ice}}(0,d)}{n_{\text{ice}} \cdot (R_{\text{air}}(0,d) + (R_{\text{ice}}(0,d))} \cdot v_{\text{eq}}t_i. \tag{34}$$
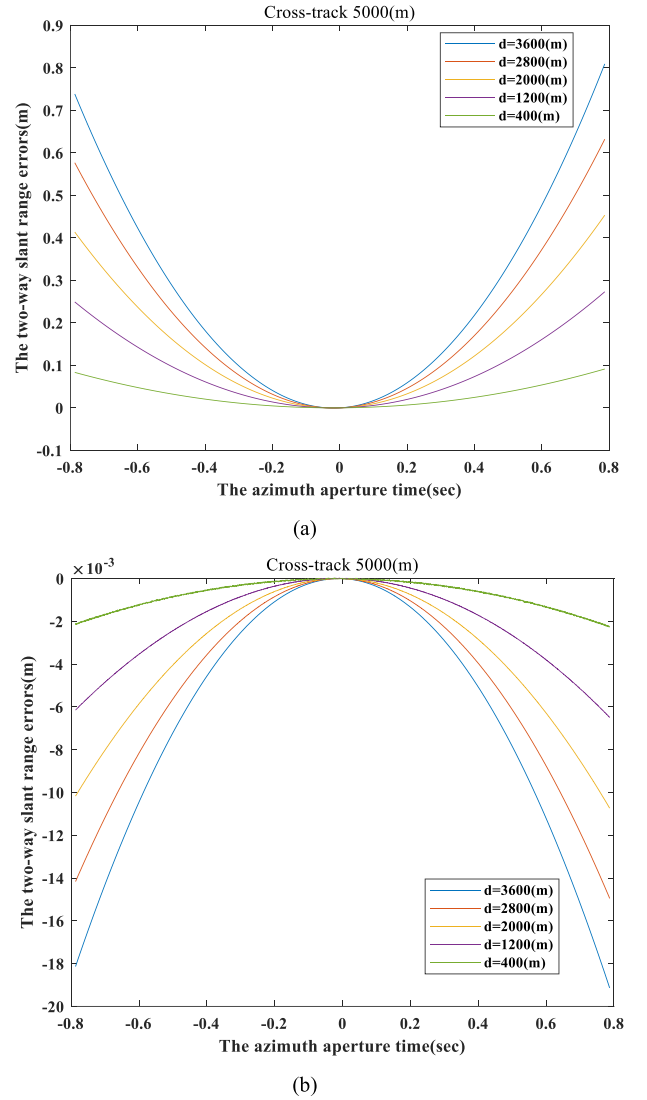

(a)

(b)

Fig. 5. Two-way slant range errors. (a) Using the equivalent slant range between a satellite and a virtual point in air. (b) Using the equivalent slant range of a new model.

The equivalent squint angle ϕ_{squ} is given by

$$\phi_{\text{squ}} = a\sin\left[\frac{R_{st}^2(t_i, d) - (R_{st}^2(0,d) + v_{\text{eq}}^2 t_i^2)}{2R_{st}(0,d)v_{\text{eq}}t_i}\right]. \tag{35}$$

In Fig. 4, the two-way equivalent slant range errors between the bistatic SAR and the five targets in ice are calculated in two ways. The bistatic SAR is composed by the master satellite and the furthest slave satellite. Referenced to the line between the Earth's center and the master satellite, the cross-track positions of five targets are 5000 m.

As shown in Fig. 5(a), five virtual points in air and five real points in ice have the same closest approaches. Comparing with the quintic equation, their two-way slant range errors at five depths (400 m, 1200 m, 2000 m, 2800 m, and 3600 m) are shown. At 2800-m depth, its two-way slant range error reaches 0.63 m, which is smaller than $\lambda/16(0.0625 \text{ m})$ [15]. At 3600-m depth, its
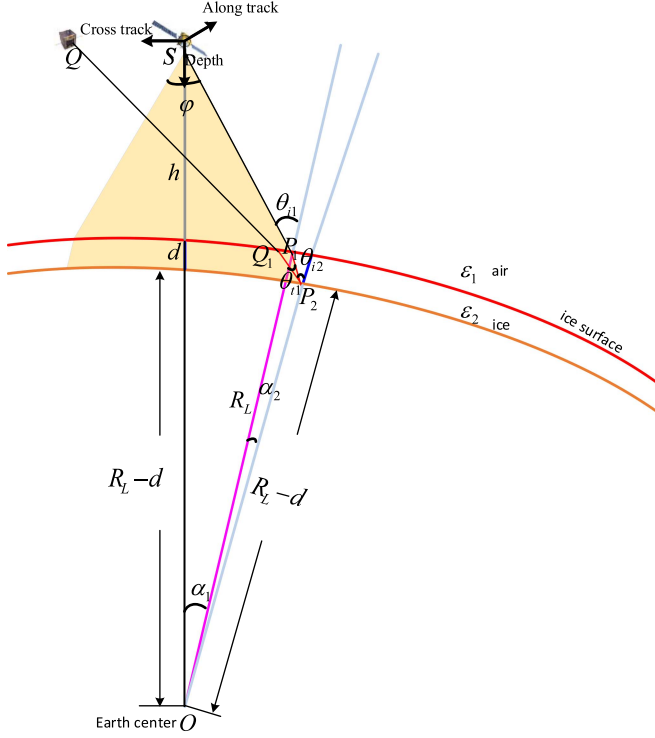
Fig. 6. Bistatic SAR geometry between two satellites and a point target in ice sheets.

two-way slant range error reaches 0.79 m, which is larger than $\lambda/16(0.0625$ m). If the depth of a point target is larger than 2800 m, this equivalent slant range model can cause image defocus.

As shown in Fig. 5(b), a new model is used to estimate the two-way slant range errors. Comparing with the quintic equation, their slant range errors at five depths (400 m, 1200m, 2000 m, 2800 m, and 3600 m) are shown. At 3500-m depth, the maximum two-way slant range error reaches 0.0182 m, which is smaller than $\lambda/16(0.0625$ m). Therefore, the new model could not cause image defocus. The quintic equation needs calculate twice for two-way slant range for the new model. Equivalent velocity, equivalent length, and equivalent squint angle also need calculate twice for two-way slant range for the new model. It reduces the computation time by using the new model.

C. Bistatic SAR Signal and Radar Data Cube

As shown in Fig. 6, the bistatic SAR geometry is given. Comparing to Fig. 5, Fig. 6 adds a receiving satellite Q.

Considering that the ice is solid ice, which has a homogeneous refractive index. At the azimuth time t_i, the receiving satellite named nk, the two-way slant range of the bistatic SAR can be expressed as

$$R_{nk}(t_i, d) = R_{nk-T\text{air}}(t_i, d) + n_{\text{ice}} \cdot R_{nk-T\text{ice}}(t_i, d)$$
$$+ R_{nk-R\text{air}}(t_i, d) + n_{\text{ice}} \cdot R_{nk-R\text{ice}}(t_i, d) \quad (36)$$

where $R_{nk-T\text{air}}(t_i, d)$, $R_{nk-T\text{ice}}(t_i, d)$, $R_{nk-R\text{air}}(t_i, d)$, and $R_{nk-R\text{ice}}(t_i, d)$ are the distances of line $\overline{SP_1}$, $\overline{P_1 P_2}$, $\overline{QQ_1}$, and $\overline{Q_1 P_2}$, respectively.

	Latitude(deg)	Longitude(deg)	Ellipsoid height (m)
P11	78.9409947087	-32.5305429135	-1959.9094715
P12	78.9409396970	-32.5070532407	-1959.9094715
P13	78.9408846853	-32.4835635680	-1959.9094715
P21	78.9409947087	-32.5305429135	-2000
P22	78.9409396970	-32.5070532407	-2000
P23	78.9408846853	-32.4835635680	-2000
P31	78.9409947087	-32.5305429135	-2040.0905285
P32	78.9409396970	-32.5070532407	-2040.0905285
P33	78.9408846853	-32.4835635680	-2040.0905285

The demodulated baseband signal of the bistatic SAR (the receiving satellite named nk) for a point target in ice can be written as

$$s_{nk}(\tau, t_i, d) = A_1 w_r \left(\tau - \frac{R_{nk}(t_i, d)}{c}\right) w_a(t_i - t_c)$$
$$\times \exp\{-j2\pi f_0 R(t_i, d)/c\}$$
$$\times \exp\left\{j\pi K_r \left(\tau - \frac{R_{nk}(t_i, d)}{c}\right)^2\right\} \quad (37)$$

where the coefficient A_1 is a complex constant; $w_r(\cdot)$ and $w_a(\cdot)$ are envelopes of range and azimuth, respectively; τ and t_i are times of range and azimuth, respectively; t_c is the beam center offset time; f_0 is the radar center frequency; c is the speed of light in free space; K_r is the frequency-modulated rate; and $R(t_i, d)$ is the two-way instantaneous slant range.

Forty bistatic SAR echo signals can be obtained for the BingSat-TOPIS system, and the radar data cube for a point target in ice can be expressed as

$$S(\tau, t_i, d) = \sum_{nk=1}^{40} s_{nk}(\tau, t_i, d). \quad (38)$$

IV. SIMULATION AND TOMOGRAPHIC IMAGING

A. Satellite Orbit

In Table I, the system parameters of BingSat-TOPIS are given. The Kepler Orbit can be explained by six Keplerian elements. There are three elements for the orientation of the orbital plane, which are inclination (i), argument of perigee (ω), and right ascension of the ascending node (Ω). The shape and size of ellipse can be defined by eccentricity (e), semimajor axis (a), and true anomaly (f). These Keplerian elements determine the satellite position in a 3-D space.

Inclination i, semimajor axis a, and eccentricity e are fixed parameters, which argument of perigee ω, right ascension of the ascending node Ω, and true anomaly f varied with the time (t). The relationship between eccentric anomaly (E) and mean anomaly (M) can be described as
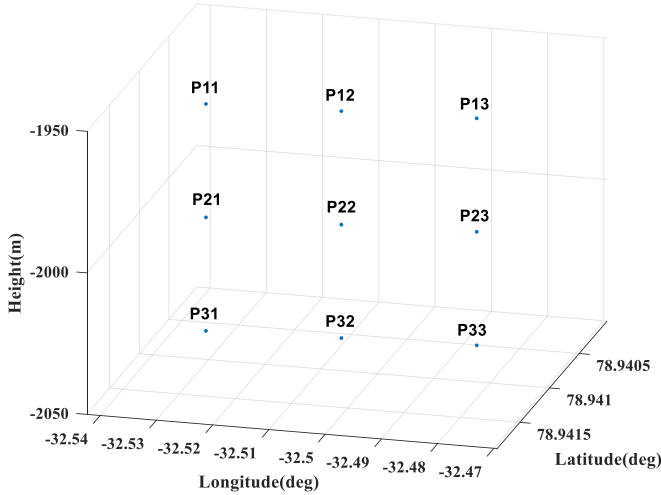
$$M = E - e \sin E. \quad (39)$$
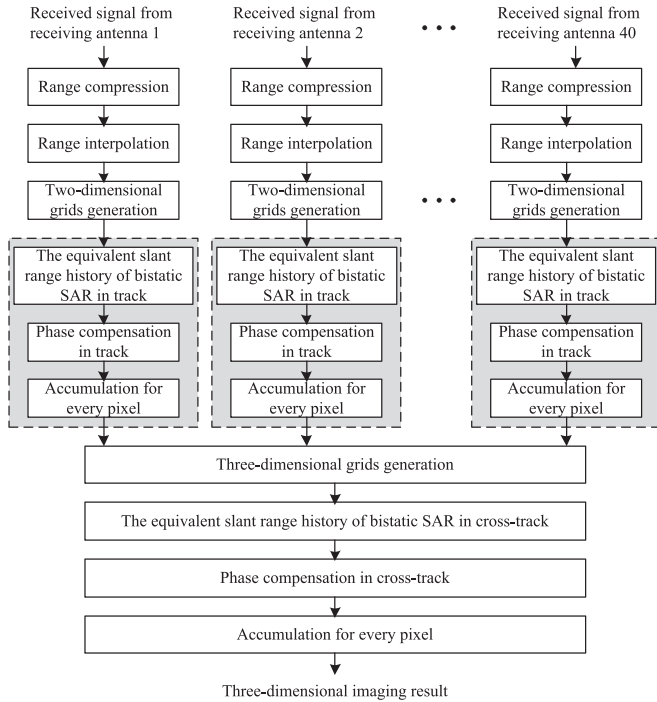
Fig. 7. Spatial positions of nine point targets.

Fig. 8. Overview of the tomographic imaging algorithm.

TABLE III
RESOLUTIONS OF NINE POINTS

	Range(m)	Track/Azimuth(m)	Cross-track (m)
P11	4.1970	17.1826	54.6875
P12	4.1970	17.1826	56.2500
P13	4.1970	17.1826	57.0313
P21	4.1343	17.1826	54.6875
P22	4.1343	17.1826	56.2500
P23	4.1343	17.1826	57.0313
P31	4.1970	17.1826	54.6875
P32	4.1970	17.1826	56.2500
P33	4.1970	17.1826	57.0313

TABLE IV
PSLR OF NINE POINTS

	PSLR in range (dB)	PSLR in azimuth (dB)	PSLR in cross-track (dB)
P11	-12.5898	-13.3176	-11.5556
P12	-12.7130	-13.3057	-12.9167
P13	-12.5427	-13.3016	-10.4789
P21	-13.0160	-13.3178	-11.5813
P22	-13.2380	-13.3053	-12.9125
P23	-13.0738	-13.3000	-10.4937
P31	-12.5099	-13.3160	-11.6038
P32	-12.7221	-13.3050	-12.9069
P33	-12.5952	-13.2975	-10.4920

The Fourier series relationship between the eccentric anomaly E and the mean anomaly M is given by

$$E = M + e \left(1 - \frac{1}{8}e^2 + \frac{1}{192}e^4 \right) \sin M$$

$$+ e^2 \left(\frac{1}{2} - \frac{1}{6}e^2 \right) \sin 2M + e^3 \left(\frac{3}{8} - \frac{27}{128}e^2 \right) \sin 3M$$

$$+ \frac{1}{3}e^4 \sin 4M + \frac{125}{384}e^5 \sin 5M. \tag{40}$$

Mean anomaly M is relate to the epoch time, which is defined as

$$M = \sqrt{\frac{\mu}{a^3}} \left(t - t_0 \right) \tag{41}$$

where $\mu = 398601.2 \mathrm{km}^3/\mathrm{s}^2$ is the Earth's gravitational constant, and a is the semimajor axis. Suppose that the satellite passes through the perigee at time $t_0 = 0$ so that

$$M = \sqrt{\frac{\mu}{a^3}} \cdot t. \tag{42}$$

Substituting (25) into (23), the eccentric anomaly E is obtained.

The relationship between the eccentric anomaly E and the true anomaly θ is given by

$$\tan \frac{\theta}{2} = \sqrt{\frac{1+e}{1-e}} \tan \frac{E}{2}. \tag{43}$$

In the orbital coordinate system, the satellite position vector can be described as

$$\begin{cases} \xi = r \cdot \cos \theta \\ \eta = r \cdot \sin \theta \\ \zeta = 0 \end{cases} \tag{44}$$

where r is the distance between the satellite and the Earth's center, and r can be written as

$$r = \frac{a(1-e^2)}{1 + e \cos \theta}. \tag{45}$$

In orbital coordinate system, the satellite velocity vector, the first derivative of the position vector (with respect to t), can be
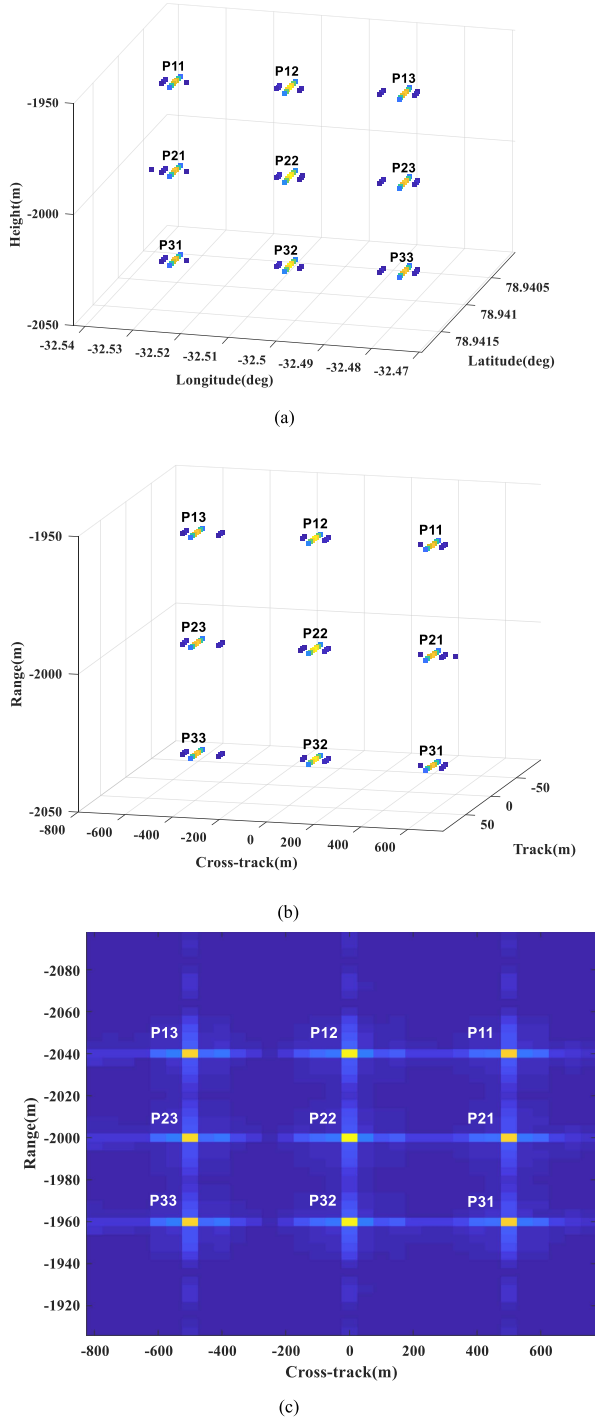
Fig. 9.   Tomographic imaging results. (a) Three-dimensional coordinate system in geodetic latitude, geodetic longitude, and height. (b) Three-dimensional coordinate system in track, cross-track, and range. (c) Two-dimensional profile (track = 0 m).
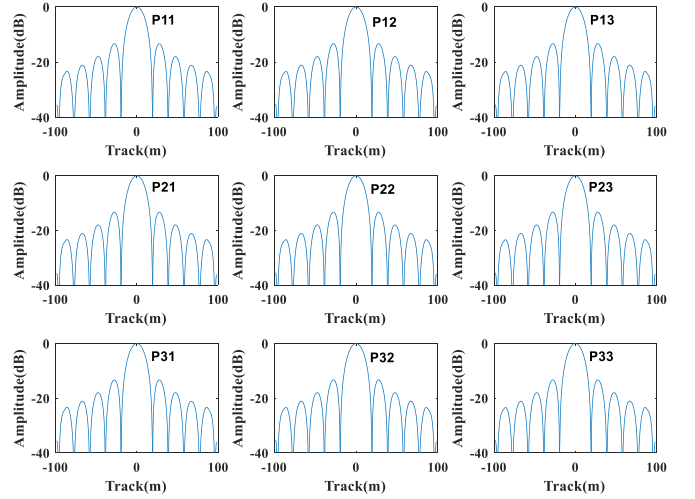

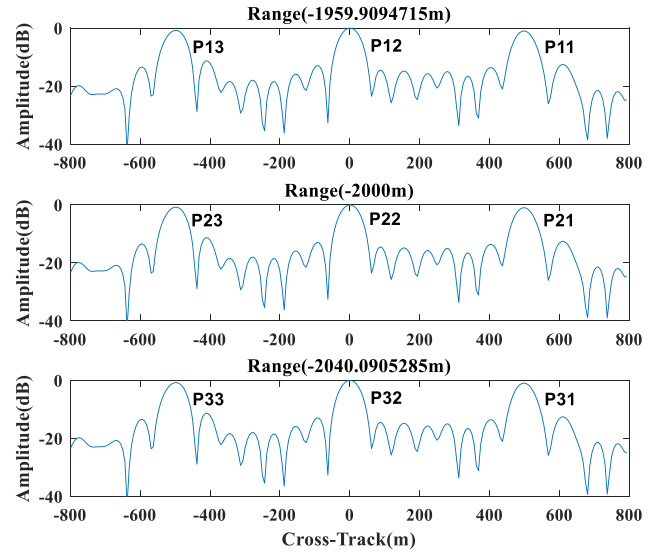Fig. 10.   Amplitudes of nine points' slices in track.

Fig. 11.   Amplitudes of nine points' slices in cross-track (the range from top to bottom are -1959.9094715 m, -2000 m, and -2040.0905285 m).

The first derivative of r , with respect to t, is given by

$$\dot{r} = r \cdot \frac{-e \sin \theta \cdot \dot{\theta}}{1 + e \cos \theta}. \tag{47}$$

Based on the motion equation of satellite, the energy of particle per unit mass, h, can be written as

$$h = r^2 \cdot \dot{\theta}. \tag{48}$$

Substituting (47) and (48) into (46), the satellite velocity can be obtained as

$$\begin{cases} \dot{\xi} = \sqrt{\frac{\mu}{a(1-e^2)}} \cdot (-\sin \theta) \\ \dot{\eta} = \sqrt{\frac{\mu}{a(1-e^2)}} \cdot (e + \cos \theta) \cdot \\ \dot{\zeta} = 0 \end{cases} \tag{49}$$

deduced by (44) as

$$\begin{cases} \dot{\xi} = \dot{r} \cdot \cos \theta - r \cdot \dot{\theta} \sin \theta \\ \dot{\eta} = \dot{r} \cdot \sin \theta + r \cdot \dot{\theta} \cos \theta \ . \\ \dot{\zeta} = 0 \end{cases} \tag{46}$$
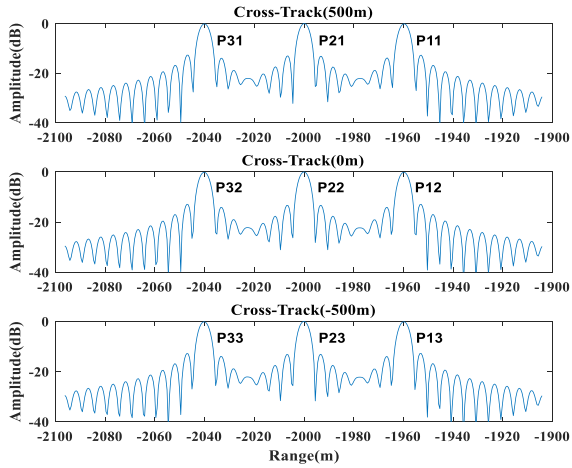
Fig. 12. Amplitudes of nine points' slices in range (the cross-track from top to bottom are 500 m, 0 m, and −500 m).

TABLE V
ISLR OF NINE POINTS

	ISLR in range (dB)	ISLR in azimuth (dB)	ISLR in cross-track (dB)
P11	-9.9478	-10.7921	-8.5717
P12	-10.1345	-10.7870	-9.4677
P13	-9.9833	-10.7883	-9.0739
P21	-9.8802	-10.7934	-8.5886
P22	-10.0723	-10.7880	-9.4762
P23	-9.9188	-10.7885	-9.0823
P31	-9.9581	-10.7905	-8.5898
P32	-10.1499	-10.7862	-9.4665
P33	-9.9862	-10.7850	-9.0784

Furthermore, the satellite acceleration, the second derivative of the position vector (with respect to t), can be obtained

$$
\begin{cases}
\ddot{\xi} = -\frac{\mu(1+e\cos\theta)^2}{a^2(1-e^2)^2} \cdot \cos\theta \\
\ddot{\eta} = -\frac{\mu(1+e\cos\theta)^2}{a^2(1-e^2)^2} \cdot \sin\theta \\
\ddot{\zeta} = 0
\end{cases}
\tag{50}
$$

Using the coordinate transform equation, the vectors of the satellite position, velocity, and acceleration are described in the ECR coordinate system. The vectors of the satellite position, velocity, and acceleration in the ECR coordinate system are $\overrightarrow{R_s}$, $\overrightarrow{V_s}$, and $\overrightarrow{A_s}$, respectively. Then

$$\overrightarrow{\mathbf{R}_s} = [x_s, y_s, z_s]^T \tag{51}$$

$$\overrightarrow{\mathbf{V}_s} = [v_{sx}, v_{sy}, v_{sz}]^T \tag{52}$$

$$\overrightarrow{\mathbf{A}_s} = [a_{sx}, a_{sy}, a_{sz}]^T. \tag{53}$$

As we know, a circle is a special kind of ellipse ($e = 0$). The master satellite of BingSat-TOPIS is a circular orbit, and the slave satellites of BingSat-TOPIS are elliptical orbits.

The system parameters of BingSat-TOPIS are listed in Table I. By using these parameters, we could simulate the orbits of the master and 40 slave satellites.

B. Scene Setting

t_c is the azimuth center time. According to Section IV-A, the vectors of the satellite position, velocity and acceleration can be calculated. Then, the master satellite's geocentric latitude and geocentric longitude of the subsatellite point at t_c are given by

$$\chi_{sm} = \tan^{-1}\left(\frac{y_{sm}}{x_{sm}}\right) \tag{54}$$

$$\phi_{sm} = \tan^{-1}\left(\frac{z_{sm}}{\sqrt{x_{sm}^2 + y_{sm}^2}}\right) \tag{55}$$

where χ_{sm} and ϕ_{sm} are the master satellite's geocentric latitude and geocentric longitude, respectively. $[x_{sm}, y_{sm}, z_{sm}]^T$ is master satellite's position. The master satellite's geocentric longitude is the same as the master satellite's geodetic longitude, but its geodetic latitude is not the same as its geodetic latitude. The master satellite's geodetic latitude can be obtained

$$\varphi_{sm} = \tan^{-1}\left[\left(1 - e_c^2 \frac{N_T}{N_T + h}\right)\tan\phi_{sm}\right] \tag{56}$$

where e_c is the Earth's eccentricity, h is the ellipsoid height, and the radius of curvature in the prime vertical N_T is given by

$$N_T = \frac{R_e}{\sqrt{1 - e_c^2 \sin\phi_{sm}}}. \tag{57}$$

Supposing that the scene's center is located under the Earth's surface 2000 m ($h = -2000$), whose geodetic latitude and geodetic longitude are the same as the subsatellite point at t_c. Therefore, the position vector of scene's center in the ECR coordinate system is given by

$$
\begin{cases}
x_t = (N_T + h)\cos\varphi_{sm}\cos\chi_{sm} \\
y_t = (N_T + h)\cos\varphi_{sm}\sin\chi_{sm} \\
z_t = \left[N_T \cdot (1 - e_c^2) + h\right]\sin\varphi_{sm}
\end{cases}
\tag{58}
$$

Many point targets could be placed in one scene, and each of them has the only position vector in the ECR coordinate system.

In order to make all the satellites just over the North Pole area, the azimuth time center $t_c = 79800$s. Nine point targets are placed below the master satellite, whose geodetic latitude, geodetic longitude, and ellipsoid height are listed in Table II.

The spatial positions of nine point targets are shown in Fig. 7. The nine point targets are all ideal points, whose backscattering coefficients equal one.

C. Tomographic Imaging Steps and Results

In Fig. 8, the tomographic imaging processing steps are illustrated. As we know, there are 40 bistatic SAR echoes for BingSat-TOPIS. First, the 40 echoes should be range compressed by using the matched filter in frequency domain. For all the 40 range compressed data, the range interpolation operation should be performed. For an imaging area, it should be divided into many 2-D grids. Back projection (BP) algorithm [16] is used in track and we obtain the 2-D image, which includes calculation of the equivalent range history of bistatic SAR by a new model, phase compensation, and accumulation to every pixel. Then, 3-D grids are generated. Finally, BP is used in cross-track by using

all the 40 2-D images and we obtain the 3-D imaging result. The BP algorithm can realize track and cross-track focusing without phase errors.

As shown in Fig. 9, the tomographic imaging results of nine point targets are displayed in two kinds of 3-D coordinate and one 2-D profile.

As we can see in Fig. 9(b), the coordinates of the nine points in track are all equal to zero. The other expression for a point is given by (cross-track, track/azimuth, and range). The point target located at scene center is (00, -2000). Compare to the scene center, the values of cross-track and track are given.

Three points in the first row are (500,0,-1959.9094715), (00,-1959.9094715), (-500,0,-1959.9094715). Three points in the second row are (500,0,-2000), (00, -2000), (-500,0, -2000). Three points in the third row are (500,0, -2040.0905285), (00, -2040.0905285), (-500,0, -2040.0905285).

To examine the responses of nine point targets in more detail, the amplitudes of nine points' slices in track/azimuth, cross-track, and range are shown in Figs. 10–12, respectively. All the three figures are shown after interpolation.

The resolutions of nine points are given in Table III. The peak sidelobe ratio (PSLR) and the integrated sidelobe ratio (ISLR) of nine points are given in Tables IV and V, respectively. All the results can meet our design indexes.

V. CONCLUSION

Tomographic imaging for orbital radar sounding of Earth's ice sheets is proposed in this article. Dozens of MirrorSAR Cube-Sats operating with SIMO mode could realize high range, track, and cross-track resolution. In this article, the ionospheric effects are ignored. In most cases (TEC value is less than 30TECU), image defocusing in track and cross-track can be ignored. Only during extreme ionospheric activity, it is necessary to consider ionospheric compensation by one value in track. By using the matched filter in the frequency domain, the range compressed data can be easily obtained. Then, the BP algorithm is used in both track and cross-track to get the tomographic image. We deduce the equivalent slant range of a new model, which can improve the computational efficiency by using it in the BP algorithm.

ACKNOWLEDGMENT

REFERENCES

[1] E. R. Ivins, "Ice sheet stability and sea level," *Science*, vol. 324, no. 5929, pp. 888–889, May 2009.

[2] A. J. Garner et al., "Evolution of 21st century sea level rise projections," *Earth's Future*, vol. 6, no. 11, pp. 1603–1615, Nov. 2018.

[3] P. Kanagaratam, S. P. Gogineni, N. Gundestrup, and L. Larsen, "High-resolution monitoring of internal layers over the Greenland ice sheet," in *Proc. IEEE Int. Geosci. Remote Sens. Symp.*, vol. 2, 2000, pp. 460–462.

[4] X. Cui et al., "Progress and prospect of ice radar in investigating and researching Antarctic ice sheet," *Adv. Earth Sci.*, vol. 24, no. 4, pp. 392–402, Apr. 2009.

[5] J. Li et al., "High-altitude radar measurements of ice thickness over the Antarctic and Greenland ice sheets as a part of operation icebridge," *IEEE Trans. Geosci. Remote Sens.*, vol. 51, no. 2, pp. 742–754, Feb. 2013.

[6] C. Allen et al., "Antarctic ice depth sounding radar instrumentation for the NASA DC-8," *IEEE Aerosp. Electron. Syst. Mag.*, vol. 27, no. 3, pp. 4–20, Mar. 2012.

[7] M. E. Peters, D. D. Blankenship, S. P. Carter, S. D. Kempf, D. A. Young, and J. W. Holt, "Along-track focusing of airborne radar sounding data from West Antarctica for improving basal reflection analysis and layer detection," *IEEE Trans. Geosci. Remote Sens.*, vol. 45, no. 9, pp. 2725–2736, Sep. 2007.

[8] J. J. Legarsky, S. P. Gogineni, and T. L. Akins, "Focused synthetic aperture radar processing of ice-sounder data collected over the Greenland ice sheet," *IEEE Trans. Geosci. Remote Sens.*, vol. 39, no. 10, pp. 2109–2117, Oct. 2001.

[9] J. D. Paden, C. T. Allen, S. Gogineni, K. C. Jezek, D. Dahl-Jensen, and L. B. Larsen, "Wideband measurements of ice sheet attenuation and basal scattering," *IEEE Geosci. Remote Sens. Lett.*, vol. 2, no. 2, pp. 164–168, Apr. 2005.

[10] P. Xiao, W. Guo, B. Liu, L. Chen, and Z. Yu, "A spaceborne multistatic radar sounding system for the tomographic observation of polar ice sheets," *IEEE Geosci. Remote Sens. Lett.*, vol. 19, 2022, Art. no. 3502205.

[11] P. Xiao et al., "Orbital radar sounding of Earth's ice sheets: Opportunities and challenges," *J. Radars*, vol. 10, pp. 1–20, 2022.

[12] Y. Wang et al., "First demonstration of single-pass distributed SAR tomographic imaging with a P-band UAV SAR prototype," *IEEE Trans. Geosci. Remote Sens.*, vol. 60, 2022, Art. no. 5238618.

[13] M. Liu and P. Xiao, "A fast, three-dimensional, indirect geolocation method using IAGM and DSM data without GCPs for spaceborne SAR images," *Sensors*, vol. 19, no. 23, Nov. 2019, Art. no. 5062.

[14] B. Zhao, X. Liu, and G. Fang, "Imaging algorithm based on RMA for air borne glacier penetrating radar system," *J. Data Acquisition Process.*, vol. 25, no. 3, pp. 283–288, May 2010.

[15] C. B. Zhang, *Principles, Systems Analysis and Applications of Synthetic Aperture Radar*. Beijing, China: Science Press, 1989.

[16] L. M. H. Ulander, H. Hellsten, and G. Stenstrom, "Syntheticaperture radar processing using fast factorized backprojection," *IEEE Trans. Aerosp. Electron. Syst.*, vol. 39, no. 3, pp. 760–776, Jul. 2003.

Min Liu was born in Chongqing, China, in 1986. She received the Ph.D. degree in communication and information systems from Beihang University, Beijing, China, in 2014.

Since 2018, she has been a Senior Engineer with the Qian Xuesen Laboratory of Space Technology, China Academy of Space Technology, Beijing. Her research interests include synthetic aperture radar (SAR) image processing, SAR image quality improvement, and SAR image geolocation without ground control points. Her current research interest include tomographic imaging for radar sounding.

Peng Xiao (Member, IEEE) was born in Harbin, China, in 1984. He received the B.S. degree in communication engineering and the Ph.D. degree in communication and information systems from the School of Electronic and Information Engineering, Beihang University, Beijing, China, in 2007 and 2014, respectively.

From 2014 to 2017, he held a postdoctoral position with Beihang University. He has been a Senior Engineer with the Qian Xuesen Laboratory of Space Technology, China Academy of Space Technology, Beijing. His research interests include innovative remote sensing systems and applications based on ultrawide swath imaging with synthetic aperture radar systems, orbital radar sounder, and the development of advanced signal algorithms.

Lu Liu was born in Anhui, China, in 1988. He received the B.S. degree in information and computing science and the Ph.D. degree in applied mathematics from BeiHang University, Beijing, China, in 2010 and 2015, respectively.

He is currently an Associate Research Fellow with the Qian Xuesen Laboratory of Space Technology, China Academy of Space Technology, Beijing. His current research interests include compressed sensing, pattern analysis and machine learning, hyperspectral remote sensing, and radar signal processing.

Chunzhu Yuan was born in Linyi, China, in 1987. He received the master's degree in instrumentation science and technology from Beihang University, Beijing, China, in 2011.

Since 2011, he has been an Engineer with DFH Satellite Co., Ltd., Beijing. His research interests include spacecraft system design and satellite computer design.

Xiaohong Sui was born in Yining, Xinjiang, China, in 1988. She received the Ph.D. degree in spacecraft design from the China Academy of Space and Technology, Beijing, China, in 2017.

Since 2017, she has been a Junior Researcher with the Qian Xuesen Laboratory of Space and Technology, Beijing. Her research interests include ocean altimetry satellite system design and data application of ocean gravity inversion and bathymetry prediction.